Effect of placement configuration on the microstructure, porosity and mechanical performance of dissimilar remote laser welding of additive manufactured AlSi10Mg alloy and conventionally manufactured 1050 aluminium sheets

Tianzhu Sun[a1*], Conghui Liu[b1], Pasquale Franciosa[a], Nesta Ferguson[c], Gregory Gibbons[a], Dariusz Ceglarek[a], Evans Mogire[d], Peilei Zhang[e]

[a]*WMG, University of Warwick, Coventry, CV4 7AL. UK*

[b] *School of Materials, The University of Manchester, Manchester, M13 9PL, UK*

[c] *School of Engineering, University of Warwick, Coventry, CV4 7AL. UK*

[d] *Buehler, WMG Materials Engineering Centre, the University of Warwick, Coventry CV4 7AL, UK*

[e] *School of Materials Science and Engineering, Shanghai University of Engineering Science, Shanghai 201620, China*

** Corresponding author, E-mail address:Tianzhu.sun@warwick.ac.uk*

[1] *These authors contributed equally to this work.*

Abstract

Additive manufacturing (AM) has gained significant attention in automotive applications, while the low weldability of AM material poses challenges when assembling AM materials with conventionally manufactured materials. This study investigated the laser welding of AM AlSi10Mg and AA1050 sheet metal in an overlap configuration, focusing on the impact of placement configuration of two materials on weld properties. This aims to provide valuable insights for optimizing the localized geometry of AM components to enhance joint performance. Results showed that positioning AM AlSi10Mg on top leads to a higher weld penetration and higher Si content within the molten pool, especially in the upper sheet. Additionally, weld zone grain structure was greatly influenced by alternating the placement configuration, where welds with AM AlSi10Mg on top exhibiting more equiaxed grains in the weld centre and refined columnar grains near the fusion boundary of upper sheet. Furthermore, significantly reduced weld porosity was determined by positioning AM AlSi10Mg at the bottom (3.2±0.4%~7.1±0.9%) compared to placing it on top (16.9±0.9%~20.1±0.9%) in all scenarios ranging from full penetration to partial penetration. This can be related to the fact that the hydrogen bubbles originating from AM AlSi10Mg experienced a shorter exposure in the molten pool, limiting the merging and growth of small bubbles. However, a slightly lower joint strength was determined in welds with AM AlSi10Mg at the bottom which may be due to the plastic deformation incompatibility between large columnar grains in the fusion zone and the fine grains in the as-printed material.

Keywords: Additive manufactured alloy, Laser welding, Overlap joint, Porosity, mechanical performance

1. Introduction

Aluminium alloys produced through the Laser Powder Bed Fusion (LPBF) technique has gained substantial attention in the automotive and aerospace sectors [1,2] due to the promising design flexibility and reduced material waste [3], while retaining the inherent advantages of aluminium alloys, such as high strength-to-weight ratio and excellent thermal conductivity [4]. AlSi10Mg has been extensively investigated for the additive manufacturing (AM) process due to its ease of processing and unique combination of properties, including high structural durability, good corrosion resistance and reliable high-temperature stability [5,6]. Various applications of AM AlSi10Mg alloy have been reported in the automotive industry, for example transmission pump housings [3], electrical windings [1] and battery box gussets [2]. Despite the advantages of AM AlSi10Mg, a critical challenge lies in the scalability of the AM parts, primarily limited by the low build volume capability. A recent study has indicated that the machine cost of the LPBF technique increases exponentially with the maximal part build length [7].

Joining of AM components as a post-AM process represents a potential approach to overcome dimensional limitations, and various welding techniques have been proposed in recent studies. Du et al. [8,9] and Moeini et al. [10] demonstrated friction stir welding of AM AlSi10Mg alloy in the butt configuration, illustrating that a defect-free weld can be achieved with sufficient heat input, i.e. by increasing rotation speed. Furthermore, they suggested that the welding direction relative to the build direction of the AM process significantly influences the fatigue performance, with the best results determined when the welding direction is parallel to the build direction. Nahmany et al. [11,12] discussed the use of electric beam welding for joining AM AlSi10Mg alloy in the butt configuration and claimed that a joint strength close to the base material but with a slight loss in ductility due to the weld porosity. Zhang et al. [13] investigated tungsten inert gas (TIG) welding of AM AlSi10Mg alloy in the butt configuration and observed frequent presence of pores in the weld zone, with larger pores concentrated near the fusion boundary.

More recently, laser beam welding has been proposed for joining AM alloys due to its superior performance in processing speed, processing flexibility and energy density compared to the aforementioned welding techniques [14–16]. Zhang et al. [13] reported a significant improvement in the joint strength of AM AlSi10Mg laser welds compared to TIG welds. As discussed in [17,18], the dominant challenge in laser welding of AM alloy is the high susceptivity to porosity resulting from two factors: (1) the growth and coalescence of pre-existing micro pores in the AM components, and (2) the precipitation of dissolved hydrogen originating from the oxide films of the raw powder. Chen et al. [12] reported that laser welding in the high-pressure environment could significantly reduce weld porosity since the growth and merging of micro-pores were much restricted. Vincenzo et al. [19] demonstrated that increasing welding speed while keeping a constant laser power is effective for reducing weld porosity. However, to the author's best knowledge, no studies have been conducted on the overlap laser welding of AM AlSi10Mg alloy and conventionally manufactured aluminium alloy. For the overlap welding of dissimilar materials, the placement configuration of upper and lower plate is one of the factors influencing the weld quality, with the asymmetrical characteristic of the weld zone being more apparent than in the case of butt welding. It should be noted that the study by Chen et al. [20] on the dissimilar laser welding of conventionally manufactured 5082 and 6061 aluminium alloys has identified significant

variation in crack sensitivity, porosity distribution and joint strength when exchanging the placement position of two materials under the same welding parameters.

In this view, the present study focuses on investigating the impact of exchanging the position of AM AlSi10Mg sheet and conventionally manufactured 1050 aluminium sheet during an overlap laser welding process. A remote laser welding system equipped with adjustable ring mode (ARM) laser source was employed, without the utilisation of filler wire and shielding gas throughout all experiments. Laser beam oscillation with different oscillation widths, while maintaining the laser power, was utilised to produce welds ranging from full penetration to partial penetration. This allows for various levels of material melting in the lower part and, consequently, created a more pronounced difference between the two placement configurations. Evolutions of porosity distribution, weld grain structure, elements distribution and joint mechanical strength were characterised and discussed. The aim of this research to provide valuable insights for designing the localised geometrical feature of the AM components when joining with conventionally manufactured material in the overlap configuration is required during the industrial assembly process.

2. Experimental details

2.1 Additive manufacturing of AlSi10Mg alloy

The AlSi10Mg powder employed in this study was provided by Carpenter Additive (UK) and has a nominal composition (in wt. %) of 9-11% Si, 0.2-0.4% Mg, ~0.45% Mn, ~0.55% Fe, ~0.15% Ti, ~0.1 %Zn, with the balance as Al. The LPBF process was performed using an EOSintM 280 LPBF 3D printer (EOS GmbH, Germany) in an argon atmosphere, equipped with a 400 W Yb:YAG laser. The printing process maintained a constant laser power of 340 W, scanning speed of 1300 mm/s, and layer thickness of 30 µm. 120 samples were built in one batch with dimensions of 40 mm (width) × 2.5 mm (thickness) × 70 mm (height). Following the printing process, samples were heat-treated at 250 ℃ for 2 hours to release residual stresses.

2.2 Characterisation of base materials

X-ray Computed Tomography (X-ray CT) was utilised to characterise the interior microstructural porosity of the AM AlSi10Mg samples. The scans were conducted using the Versa 620 (Carl Zeiss Ltd, UK) with a voxel size of 6 µm, an exposure voltage of 80 kV and an exposure time of 5 s on six samples, each having the dimension of 40 mm (width) × 2.5 mm (thickness) × 23 mm (height). The acquired images were reconstructed and analysed using the Avizo 2021.2 software (Carl Zeiss Ltd, UK).

Surface morphology of the AM AlSi10Mg alloy and AA1050 sheet metal was characterised using VHX700 optical microscope (Keyence, Japan) at a magnification of ×200 and scanning step size of 2 µm in the depth direction. The area roughness parameter, S_a, was employed for the evaluation of surface roughness.

2.3 Remote laser welding process

A 10 kW Highlight FL10000-ARM fibre laser (Coherent, GmhH) with a wavelength of 1080 nm and a Rayleigh length of 5.3 mm was employed in this study. The laser fibre

comprises a core beam and a ring beam, with respective diameters of 100 μm and 295 μm. The laser beam was delivered by the WeldMaster Scan & Track welding head (Precitec, GmbH) with a collimation length of 150 mm and focal length of 300 mm, resulting in a spot diameter of 200 μm and 590 μm at the focal plane for the core and ring beam, respectively. The welding set-up is schematically illustrated in Fig. 1(b). An overlap welding configuration with an overlap length of 20 mm between the two sheets was used. A slot with a width of 15 mm was machined in the backplate and located well beneath the weld seam to avoid heat sinking. The AM AlSi10Mg and 1050 aluminium sheets had identical dimensions of 40 mm (width) × 2.5 mm (thickness) × 70 mm (height). Two placement configurations were employed, one with the AM AlSi10Mg positioned on top and 1050 aluminium sheet at the bottom, another one with the 1050 aluminium sheet on top and AM AlSi10Mg at the bottom. Prior to welding, the sheets were cleaned with acetone to remove surface contaminations.

During laser welding, the laser beam was tilted at 10^{o} around the y axis, perpendicular to the welding direction to prevent the back-reflection of the laser beam entering the welding head. The focal plane of the laser beam was aligned with the top surface of the upper sheet, and the welding was conducted along the x axis (parallel to the build direction of AM AlSi10Mg sheet) at an offset of 10 mm from the edge of the upper sheet. An averaged power of 2.5 kW for the core beam and 3.5 kW for the ring beam, and welding speed of 4 m/min were used for all welding trials. In addition, transverse beam oscillation with an oscillation frequency of 200 Hz and an oscillation width of 1 mm, 1.5 mm and 2 mm, was employed. No shielding gas or filler wire was utilized throughout the welding procedures. Full matrix of welding parameters employed in this study is summarized in Table 1.

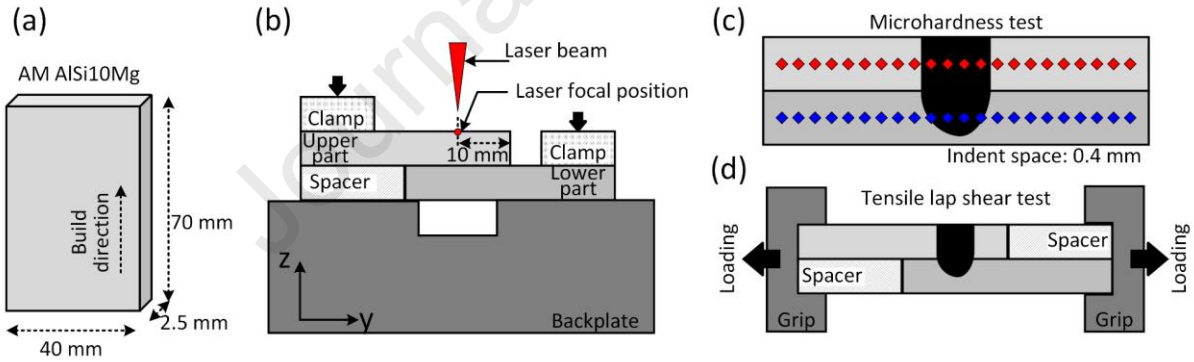

Fig. 1. Schematic diagram illustrating (a) geometry of the AM AlSi10Mg sheet (b) experimental set-up of the remote laser welding process, (c) positions of the microhardness test on the weld cross-section, and (d) set-up of the tensile lap shear test.

Table 1. Matrix of the processing parameters employed in the laser welding trials.

Experimental ID	Placement configuration	Total laser power [W]	Welding speed [mm/s]	Beam oscillation width [mm]	Energy density [J/mm^2]
#1	(Top) AM AlSi10Mg- (Bottom) AA1050	6000	67	1.0	89.6
#2	(Top) AM AlSi10Mg- (Bottom) AA1050	6000	67	1.5	59.7
#3	(Top) AM AlSi10Mg- (Bottom) AA1050	6000	67	2.0	44.8

#4	(Top) AA1050- (Bottom) AM AlSi10Mg	6000	67	1.0	89.6
#5	(Top) AA1050- (Bottom) AM AlSi10Mg	6000	67	1.5	59.7
#6	(Top) AA1050- (Bottom) AM AlSi10Mg	6000	67	2.0	44.8

In a separate welding test, the photodiode-based sensor LWM 4.0 (Precitec, Gmbh) was used to record the optical emission of the back-reflection signal with the wavelength of 1020-1090 nm at a maximum sampling rate of 50 kHz, as an indirect measurement of the laser energy absorption rate of the base material, where a stronger back-reflection signal is regarded as a lower laser energy absorption rate. Welding parameters in experiment #2 and #5 (refer to Table 1) were used. 3 measurements were conducted for each welding condition and a signal window of 0.4 s, cantered in the middle of the recorded signal (corresponding to a weld length of ~27mm) was used. Mean value, proportional to the total energy content of the emitted radiation, and the scatter level, measured by the standard deviation of the raw signal and proportional to the process instability, were used for the data analysis [21].

2.4 Weld characterisation

The welded samples were sectioned perpendicular to the welding direction using a Buehler AbrasiMet M abrasive cutter and metallographically prepared to a 0.06 μm surface finish using an AutoMet 300 Pro polisher (Buehler, USA). The cross-sectional weld geometry and area fraction of weld porosity was characterised by VHX700 optical microscope (Keyenc, Japan). The evolution of weld zone grain structure under different welding conditions was analysed by Electron Backscatter Diffraction (EBSD) using a 7800F scanning electron microscope (SEM) (JEOL, Japan), equipped with a Symmetry II EBSD detector and AZtec acquisition software (Oxford Instruments plc, UK). The average grain size was expressed by the area-weighted mean value of the equivalent diameter of individual grains using $\overline{D} = \frac{\sum W_i D_i}{\sum W_i}$, to account for the considerable scatter of individual grain size between columnar grains and equiaxed grains.

To assess the weld mechanical properties, Vickers microhardness tests were performed across the weld cross-section at the mid-thickness of upper and lower sheets (Fig. 1 (c)), using a VH3300 automatic hardness tester (Buehler, USA), with an applied load of 0.2 kg (HV0.2) for 10 s and a consistent spacing of 0.4 mm between indents. The mechanical strength of weld was determined by lap-shear tensile testing (Fig. 1 (d)) at a constant extension rate of 1 mm/min, following ISO standards [22] using a 3360 tensile machine (Instron, UK) equipped with the 30 kN load cell. Four samples having an effective weld seam length of 15 mm were tested for welding at each welding configuration and each beam oscillation width.

3. Results and discussion

3.1 Characteristics of base materials

Representative morphologies of the powders are shown in Fig. 2 (a) and an average diameter of 26 μm was determined. Fig. 2(b) shows the representative 3D reconstructed images of the part produced by LPBF process using the powder

demonstrated in Fig. 2 (a). Micro pores and residual particles were revealed in the AM AlSi10Mg sheet, whose equivalent diameters are in the range of 19 - 40 µm and 25 - 60 µm, respectively. Furthermore, an averaged volume fraction of micro pores at 0.029±0.005% and residual particles at 0.023±0.006% were determined among the six tested samples.

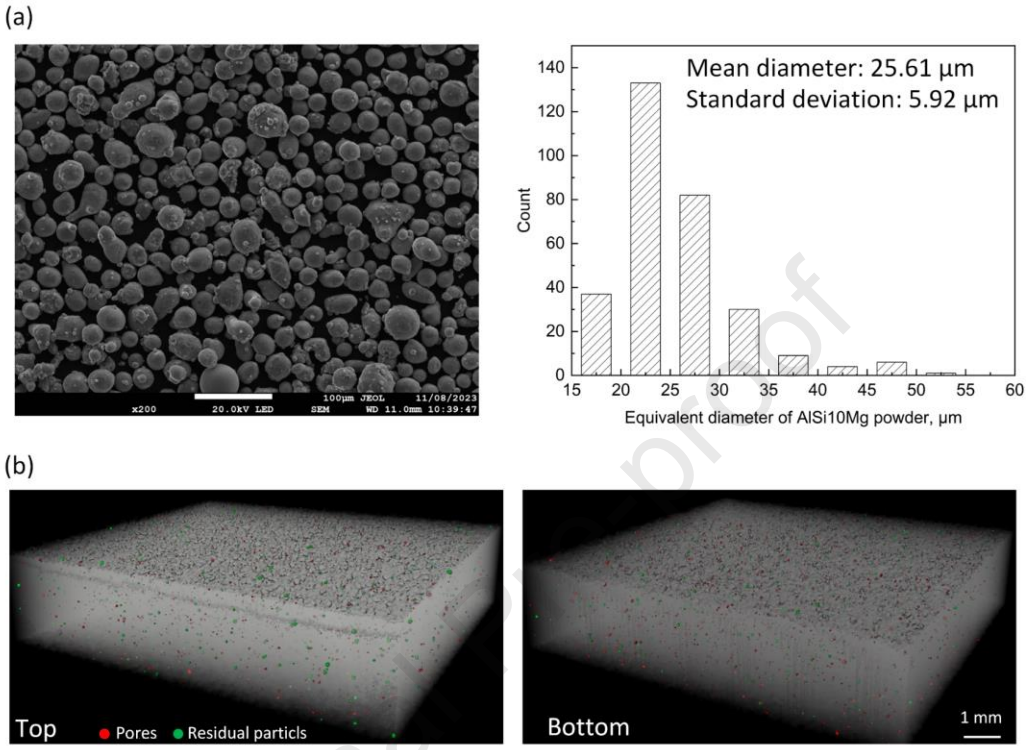

Fig. 2. (a) Representative morphologies of the AlSi10Mg powder used in this study, with the powder size distribution, and (b) Representative reconstructed 3D images of the AM AlSi10Mg sheet employed in this study: (left) top part of the built and (right) bottom part of the built.

One significantly different characteristic between the AM AlSi10Mg alloy and AA1050 sheet prior to welding is the surface roughness, which plays an important role in the laser energy absorption rate and consequently the characteristics of the molten pool, i.e., geometry and stability [23]. Fig. 3 shows the optical images of the external surface of two base materials and contour maps demonstrating the surface morphology. It can be seen clearly that a rougher surface was identified in AM AlSi10Mg, with noticeable bumps and depressions, which as a result, leads to much higher area surface roughness of 20.7 µm as compared to the AA1050 sheet exhibiting an area surface roughness of 0.6 µm. Therefore, a relatively higher laser energy absorption rate is expected in AM AlSi10Mg [23]. This can be further evidenced by the back-reflection signal as shown in Fig. 4 where a relatively lower mean value was determined when AM AlSi10Mg was position on top, suggesting that less laser energy was reflected by the material.

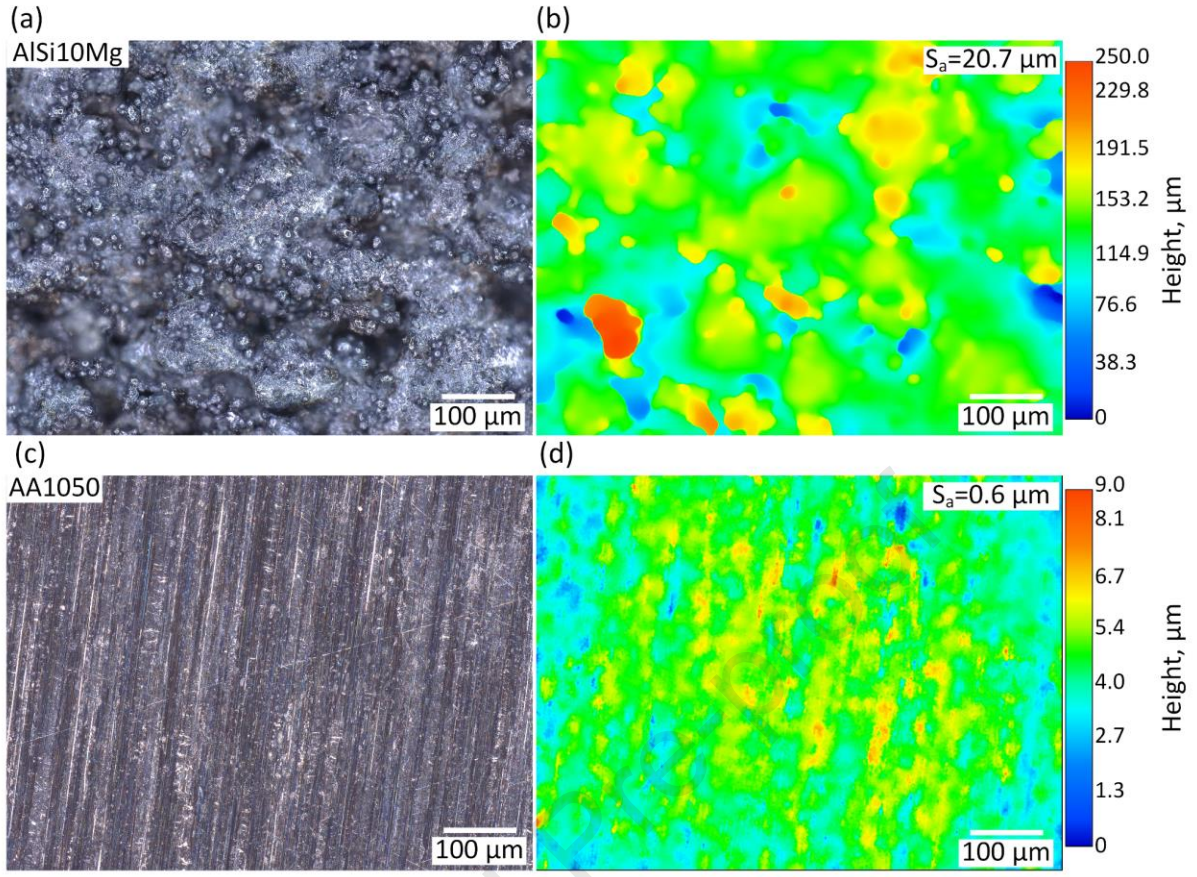

Fig. 3. Surface optical images of the base material used in this paper: (a) AM AlSi10Mg alloy and (c) AA1050 sheet metal, and contour maps showing the surface morphology of (b) AM AlSi10Mg alloy and (d) AA1050 sheet metal.

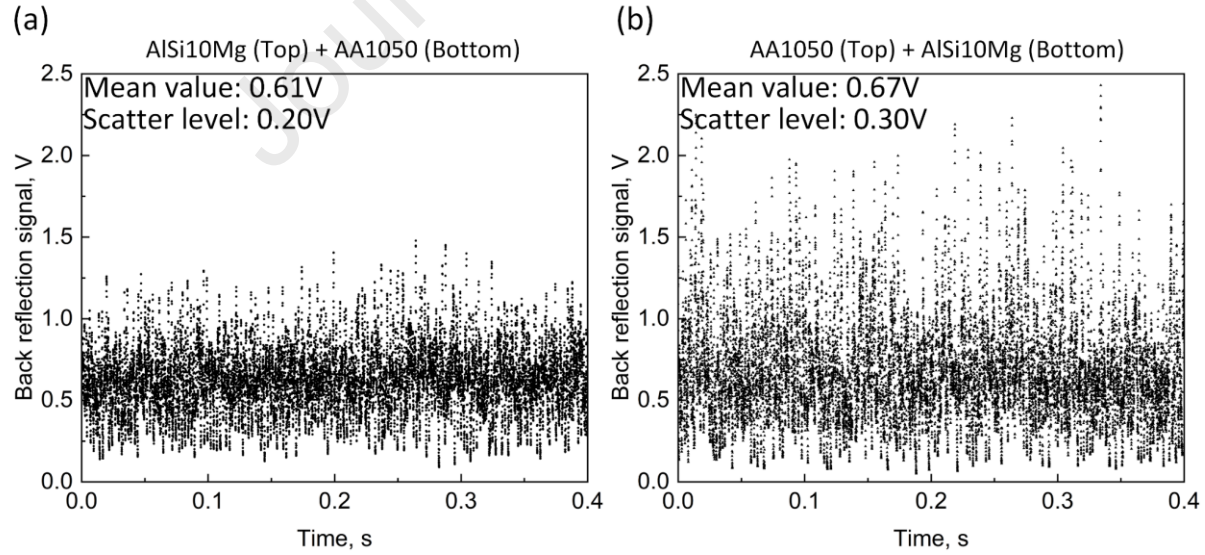

Fig. 4. Representative back-reflection signal recorded during the laser welding with placement configuration (a) AM AlSi10Mg sheet on the top and AA1050 sheet at the bottom, and (b) AA1050 sheet on the top and AM AlSi10Mg sheet at the bottom. The welding parameters in (a) and (b) refer to the experiment #2 and #5 in Table 1, respectively.

3.2 Weld zone macrostructures and porosity distribution

Fig. 5 illustrates representative optical images of weld cross-sections produced with different placement configurations and oscillation widths, where the fusion boundary is addressed by the white dashed line. The evolution of weld geometrical parameters including the weld penetration and weld width at interface is summarized in Fig. 6(a) and (b). Overall, the weld penetration decreases and the weld width at the interface increases as beam oscillation width increases, due to a more diffused laser energy distribution and a reduced peak energy intensity [15]. Furthermore, it is evident that for a given oscillation width, the weld penetration is slightly higher when the AM AlSi10Mg sheet is positioned on top, compared to the scenario where the AA1050 sheet is on top. This difference can be attributed to the higher laser energy absorption rate of the AM AlSi10Mg sheet owing to a higher surface roughness as described in Fig. 3 [23] and confirmed in Fig. 4 .

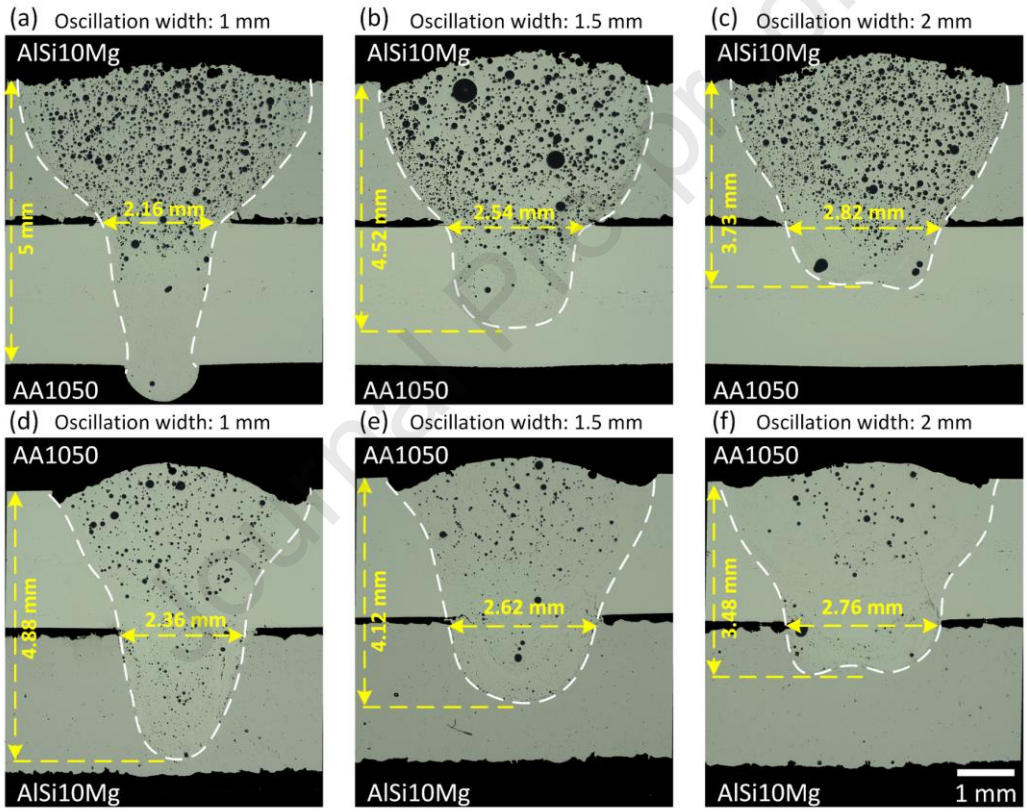

Fig. 5. Representative optical images of weld cross-section produced at the oscillation width of (a) and (d): 1 mm, (b) and (e) 1.5 mm, and (c) and (f) 2 mm. In (a-c) AlSi10Mg sheet was positioned on the top and in (d-f) AA1050 sheet was positioned on the top. The white dashed line sketched the fusion boundary.

Fig. 5 also reveals the presence of weld porosity in all cases, with the statistical analysis of the weld porosity presented in Fig. 6 (c) and (d). Note that the analysis was conducted exclusively on pores with an equivalent diameter exceeding 20 μm to mitigate the disruption from background noises in optical images. For both placement configurations, pores are distributed throughout the entire weld zone with a substantially greater number of pores and larger pore diameter observed in the upper sheet. It is also evident that by alternating the position of AM AlSi10Mg sheet from the

top to the bottom, significant reduction of weld porosity can be obtained, as evidenced by the drop of total area fraction and the quantity of pores in Fig. 6. The underlaying mechanism will be discussed later in this section.

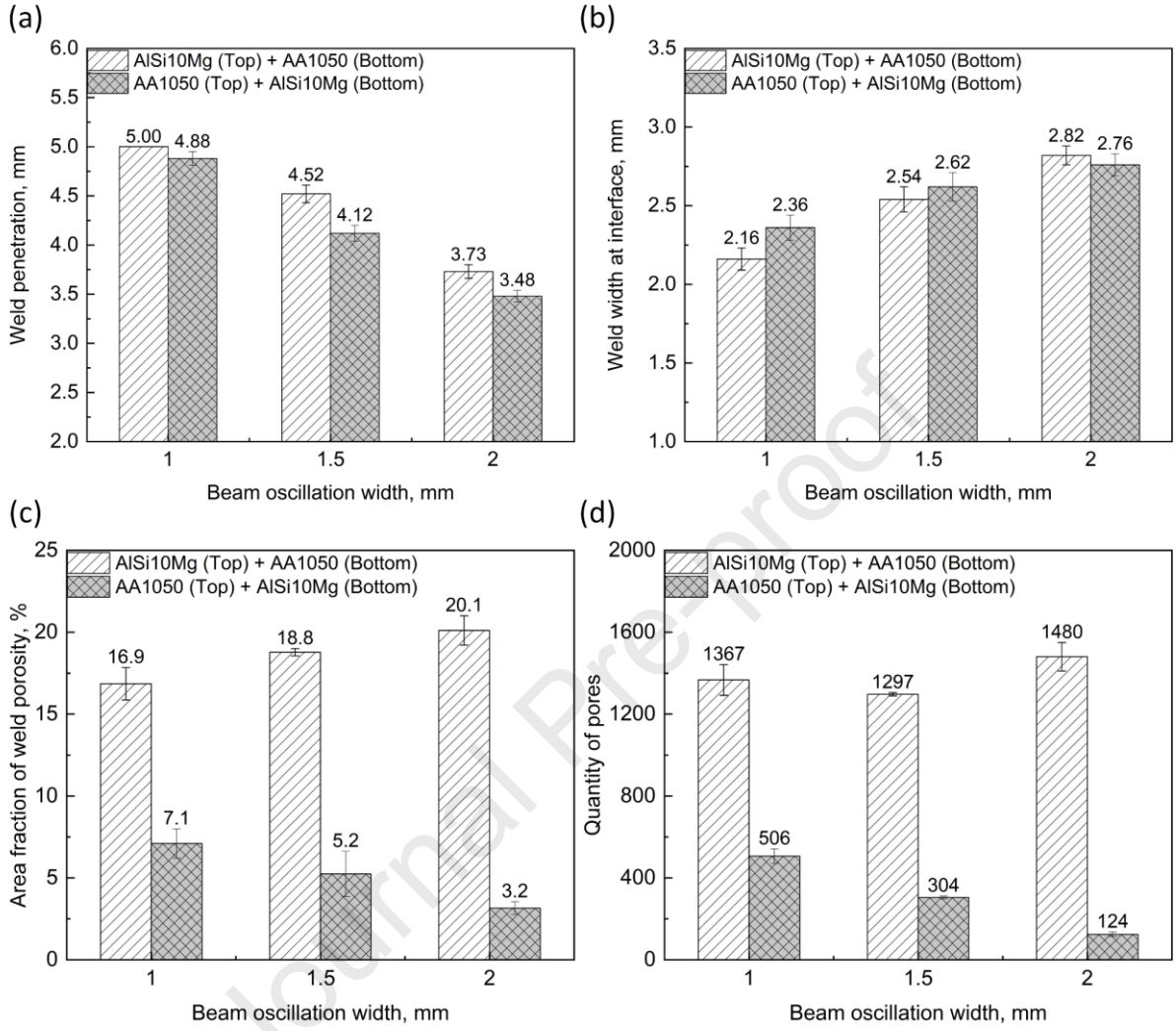

Fig. 6. Quantitative summary of (a) weld penetration, (b) weld width at interface, (c) area fraction of weld porosity and (d) quantity of pores from the optical images of weld cross-section produced at different beam oscillations and placement configurations. Note that pores with the equivalent diameter of more than 20 µm were investigated in (c) and (d).

3.3 Weld zone grain structure and chemical composition distribution

The evolution of grain structure in welds produced at different placement configurations and various oscillation widths was characterized by EBSD on the transverse cross-section and the results are presented in Fig. 7, with the statistical summary of the area-weighted mean grain size in Fig. 8. In all cases, columnar grains were observed originating from the fusion line and growing towards the weld centre, following the direction of the maximum thermal gradient, while equiaxed grains were determined in the weld centre. This observation aligns with previous studies on the remote laser welding of conventional manufactured aluminium alloys [15,16] and AM aluminium alloys [18]. In addition, as the beam oscillation increases, there is an observable increase in the mean grain size within the entire weld zone (Fig. 8 (a)) and this

phenomenon is closely related to the evolution of grain size in the weld zone of the upper sheet (Fig. 8 (b)).

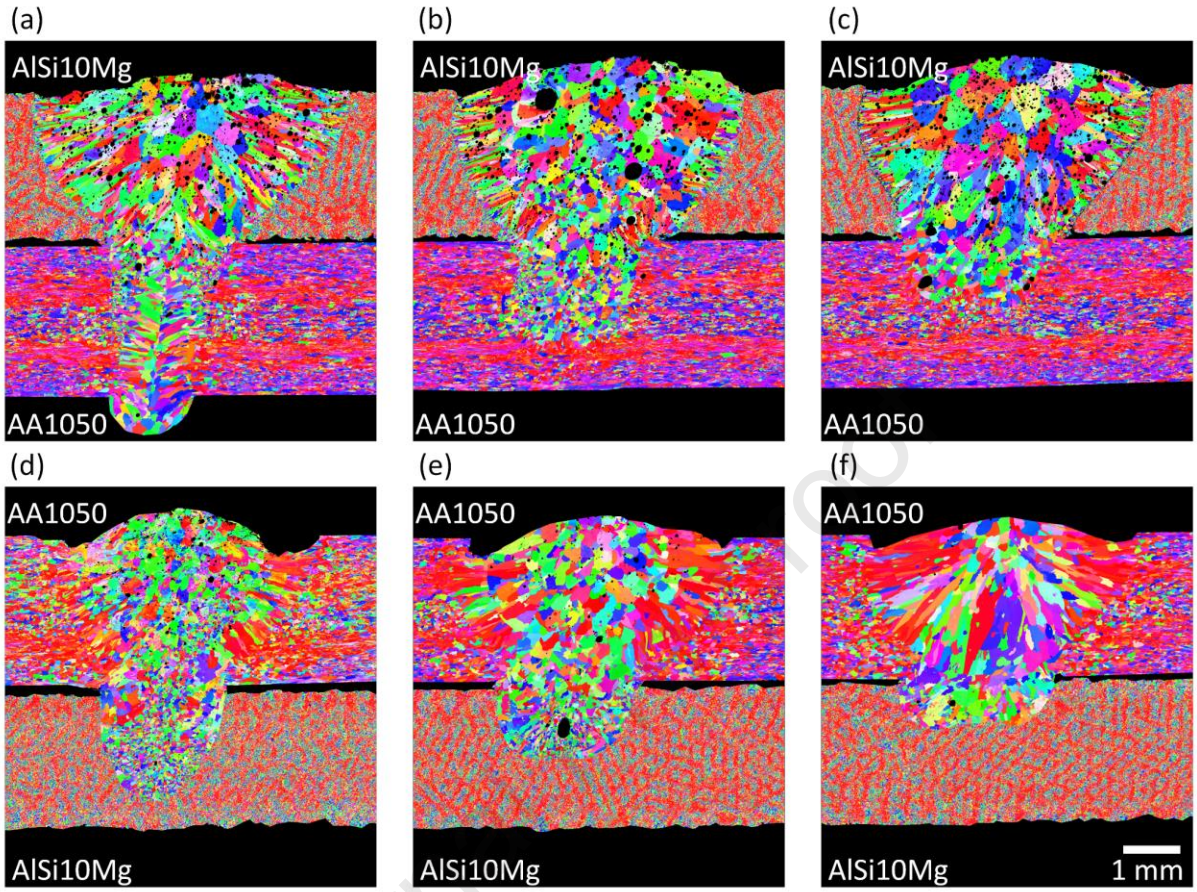

Fig. 7. Representative EBSD map of weld cross-section produced at the oscillation width of (a) and (d): 1 mm, (b) and (e) 1.5 mm, and (c) and (f) 2 mm. In (a-c) the AlSi10Mg sheet was positioned on the top and in (d-f) the AA1050 sheet was positioned on the top.

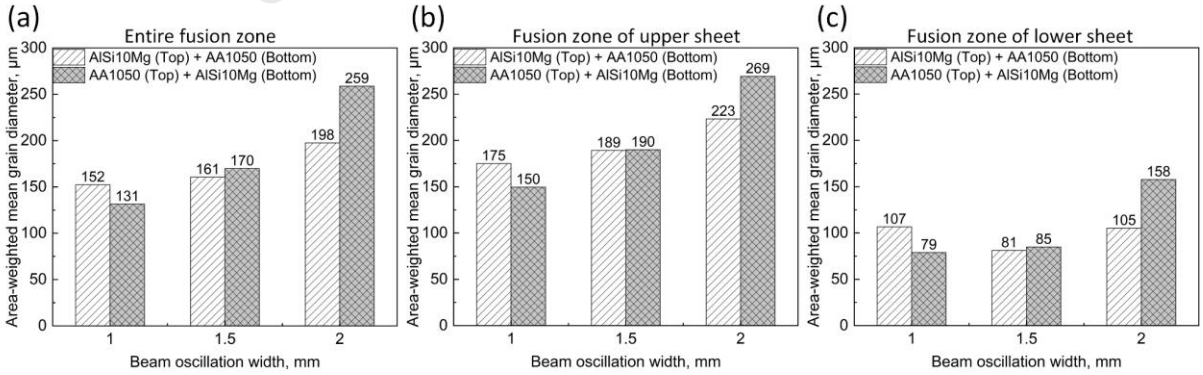

Fig. 8. Comparison of fusion zone grain size in welds produced with different placement configuration: (a) entire fusion zone, (b) fusion zone of the upper sheet and (c) fusion zone of the lower sheet. Note that grain size is expressed by the equivalent diameter of the circle with an area equal to the grain.

Several distinctive phenomena were identified when comparing the two placement configurations. When the AM AlSi10Mg sheet was positioned on top, thinner columnar

grains near the fusion boundary of the upper sheet are observed, in contrast to the case where the AA1050 sheet was on top. Furthermore, more equiaxed grains, but with greater diameter were determined in the fusion zone of the upper sheet when the AM AlSi10Mg sheet was positioned on the top, and this is more pronounced as beam oscillation width increases. Previous studies [24–26] have reported that the increasing silicon content within the molten pool greatly influences the solidification behaviour by restricting the grain growth, which results in finer dendrites. Therefore, the distribution of Si content in the depth direction was characterised by SEM-EDX in both placement configurations and the results are plotted in Fig. 9. A notable migration of Si content from the AM AlSi10Mg sheet to the AA1050 sheet was identified and its extent is greater as the beam oscillation width increases. Overall, a greater level of Si content was determined in the fusion zone of the upper sheet when the AM AlSi10Mg sheet was positioned on top, explaining the presence of thinner columnar grains near the fusion boundary. Furthermore, it has been reported in [24,25] that the addition of Si may facilitate the constitutional undercooling of the molten material during solidification, therefore a larger proportion of equiaxed grains were identified in Fig. 7 (c) as compared to Fig. 7 (f). The relatively larger size of equiaxed grains in the weld centre of the upper sheet in Fig. 7 (a-c) as compared to Fig. 7 (d-e) can be attributed to the longer solidification time that the molten material experienced due to the higher peak temperature associated with the higher laser energy absorption rate of the AM AlSi10Mg sheet as discussed in Fig. 4, leading to a greater extent of grain growth in the former case.

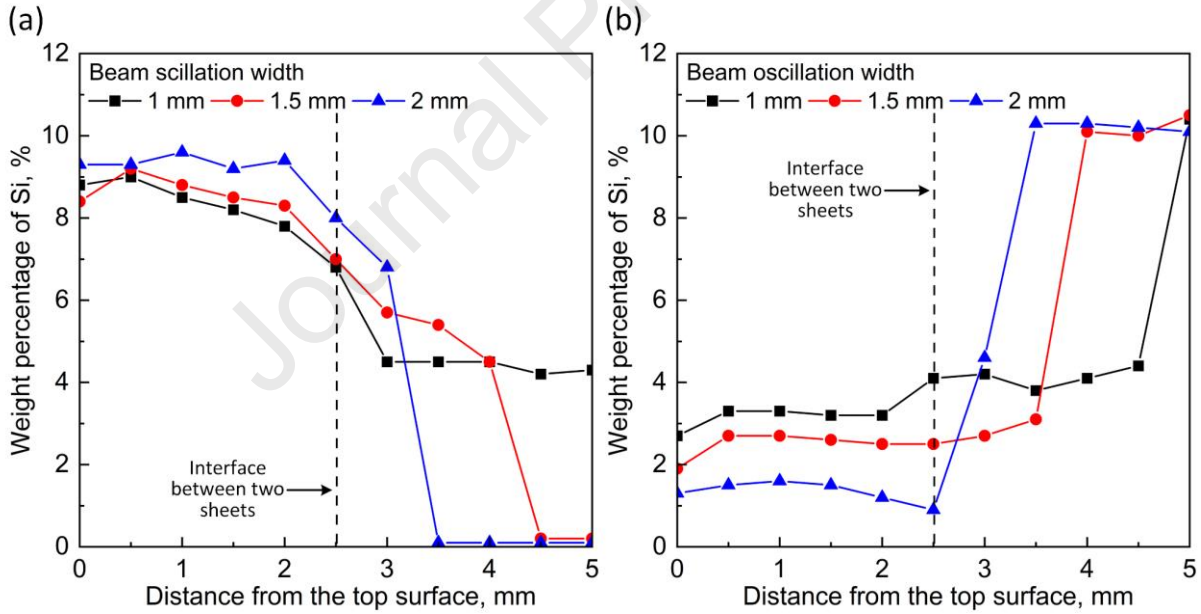

Fig. 9. Evolution of the weight percentage of the Si content in the depth direction for welds produced with different beam oscillation width in the placement configuration of (a) AM AlSi10Mg sheet on the top and AA1050 sheet at the bottom, and (b) AA1050 sheet on the top and AM AlSi10Mg sheet at the bottom. Note that the black dashed line indicates the position of interface between two sheets.

3.4 Microhardness distribution and mechanical strength

Fig. 10 illustrates the hardness profiles across the weld zone, measured at the mid-thickness of both the upper sheet and lower sheet (as described in Fig. 1(c)). The base

materials, AM AlSi10Mg and AA 1050, exhibited hardness values of 95±2 HV0.2 and 40±1 HV0.2, respectively. It should be noted that the vertical dashed lines in Fig. 7 indicate the fusion boundary at the mid-thickness of sheets (red for upper sheet and blue for the lower sheet). The evolution of hardness within the fusion zone can be primarily attributed to the development of grain structure and the strengthening precipitates [27]. Grain coarsening was observed in the fusion zone of both materials as compared to the fine microstructure of corresponding base materials as shown in Fig. 7, which results in a reduction of hardness. Additionally, the migration of Si content from the AM AlSi10Mg sheet to the AA1050 sheet leads to the redistribution of the eutectic and primary silicon crystals, where an increase in Si content is expected to correlate with greater hardness as reported in [28,29]. Consequently, a reduction in hardness is observed within the fusion zone of the AM AlSi10Mg sheet, while an increase in hardness is noted within the fusion zone of AA1050 sheet. As the beam oscillation width increases, a further drop of hardness is observed in the fusion zone of the upper sheet for both placement configurations, predominantly induced by the grain coarsening as shown in Fig. 7 and 8.

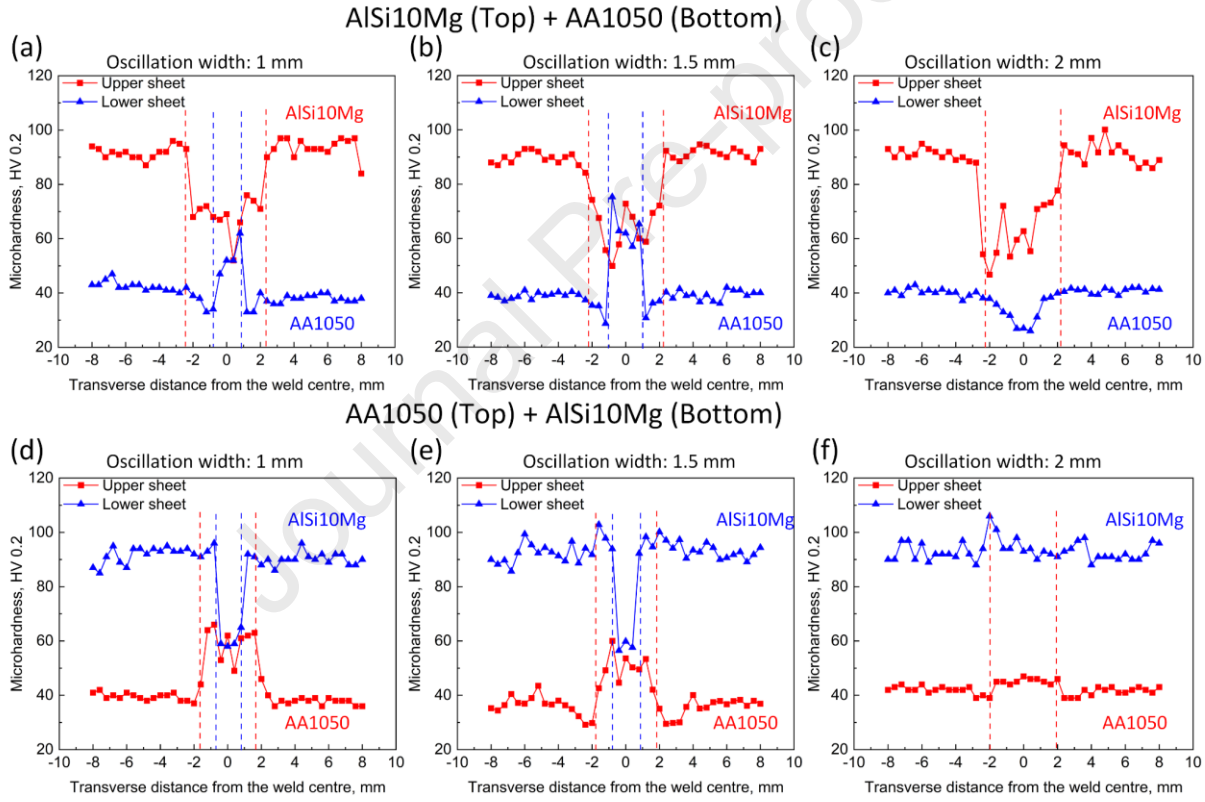

Fig. 10. Microhardness distribution of weld produced at the oscillation width of (a) and (d): 1 mm, (b) and (e) 1.5 mm, and (c) and (f) 2 mm. In (a-c) AlSi10Mg sheet was positioned on the top and in (d-f) AA1050 sheet was positioned on the top. Note that line measurements were conducted at the mid-thickness of the upper sheet and lower sheet, respectively (see Fig. 1 (c)). The red and blue dashed lines indicate the position of the fusion boundary at the corresponding measurement line.

The mechanical strength of welds during the lap-shear tensile test is illustrated in Fig. 11 (a), expressed by the maximum linear load, with representative cross-section optical images indicating the failure position for the two placement configurations in Fig. 11 (b). In all cases, welds failed in the AM AlSi10Mg sheet regardless of the placement configuration. Failure was determined to be in the fusion zone when the AM

AlSi10Mg sheet was positioned on top, while along the fusion boundary when the AM AlSi10Mg sheet was positioned at the bottom. For both placement configurations, an increasing joint strength was determined as the beam oscillation width increased. It is interesting to see that weld joint exhibited an increasing strength as the beam oscillation width increases when the AM AlSi10Mg sheet was positioned on top, although coarser grain structure and reduced hardness were determined in the fusion zone of the AM AlSi10Mg sheet, which are generally associated with the reduction of joint strength. This observation addressees the significant impact of the weld porosity in determining the joint strength, by alternating the effective bonding area, especially in the AM AlSi10Mg sheet. As the beam oscillation width increases, an increasing effective bonding area is expected due to two factors. First the overall area fraction of pores in the AM AlSi10Mg sheet reduces as the beam oscillation width increases as shown in Fig. 6. Secondly, as seen in Fig. 11 (b), the failure path is farther from the weld centreline as the beam oscillation width increases, implying that the localised pores adjacent to the failure path tend to have smaller diameter due to faster material solidification and hence less time for the growth or coalescence of the small pores.

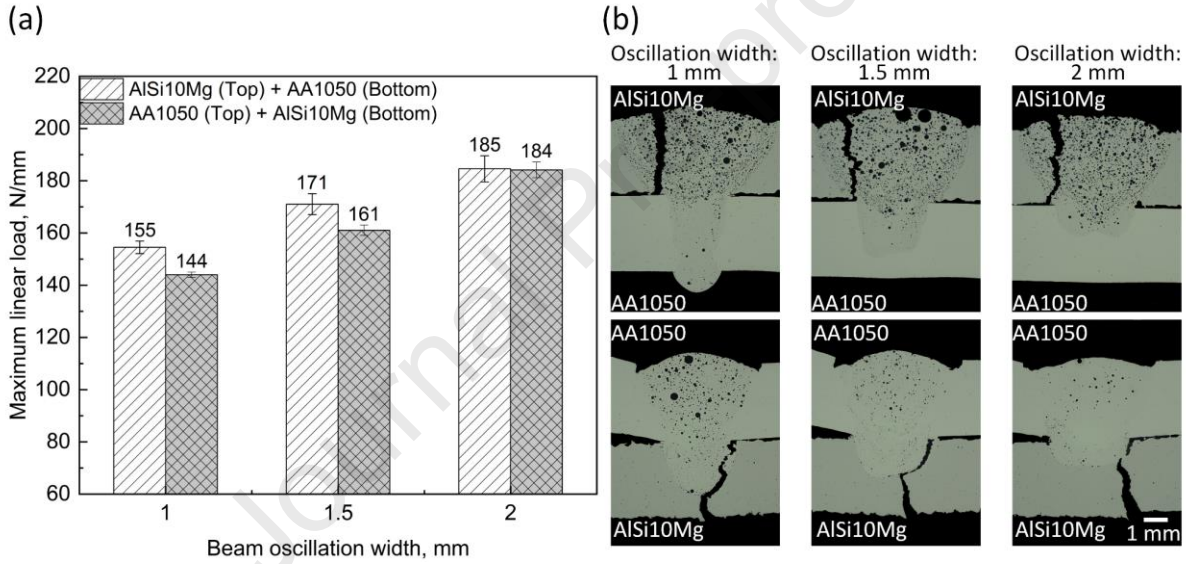

Fig. 11. (a) Comparison of the joint strength of in welds produced with different placement configuration during the tensile lap shear test, and (b) optical images of the weld cross-section showing the fracture position. Note that the joint strength is expressed by the maximum linear load.

To clarify the exact failure position, EBSD was conducted near the fusion boundary at the interface of the two sheets, as shown in Fig. 12, where the high stress concentration occurred during the lap-shear tensile test due to the geometrical constraint of the overlap joint configuration [30]. The crack propagates across the columnar grains when the AM AlSi10Mg sheet is on top, whereas it follows the grain boundary of the columnar grains at the fusion boundary when the AM AlSi10Mg sheet is at the bottom. To understand the relatively lower strength of weld with AM AlSi10Mg positioned at the bottom as compared to on top, geometrically necessary dislocations (GND) density maps were plotted in Fig. 10 (c) and (d). During the deformation of the weld joint subjected to the lap-shear tensile loading, the plastic deformation incompatibility which is generally accommodated through the development of GNDs, leads to a plastic strain gradient [31]. It can be seen that the distribution GND density

is asymmetrical between the two sides of the failure path in the weld with AM AlSi10Mg at the bottom where significant concentration of GND is observed in the side of the fusion zone owing to the distinctive grain size gradient from as-printed material to the solidified grains. This indicates a clear strain concentration in the columnar grains near the failure path, which facilitates the failure. In comparison, a relatively uniform distribution of GNDs between the two sides of failure path was observed in the weld with AM AlSi10Mg position on top (Fig. 12 (c)) due to the absence of the grain size gradient across the failure path, suggesting that the plastic deformation is accompanied evenly by the grains on both sides. Furthermore, previous studies [32–34] on the laser welding of conventionally manufactured material, where the base material has much coarser grain structure as compared to the AM material used in the current study, also identified the significant grain size gradient near the fusion boundary due to the formation of ultra fine equiaxed grains along the fusion line and revealed the weak bonding between the fine and coarse grains. Although the formation of ultra fine equiaxed grains were suggested to be mitigated in the joining of conventional manufactured materials, it is assumed to be beneficial for the joining of AM material for a smoother grain size gradient so as to reduce the plastic deformation concentration. Approaches associated with the formation of equiaxed grains near the fusion boundary such as the addition of alloying elements [32], utilisation of beam shaping technique [16] and beam oscillation techniques [33] will be further investigated in the future.

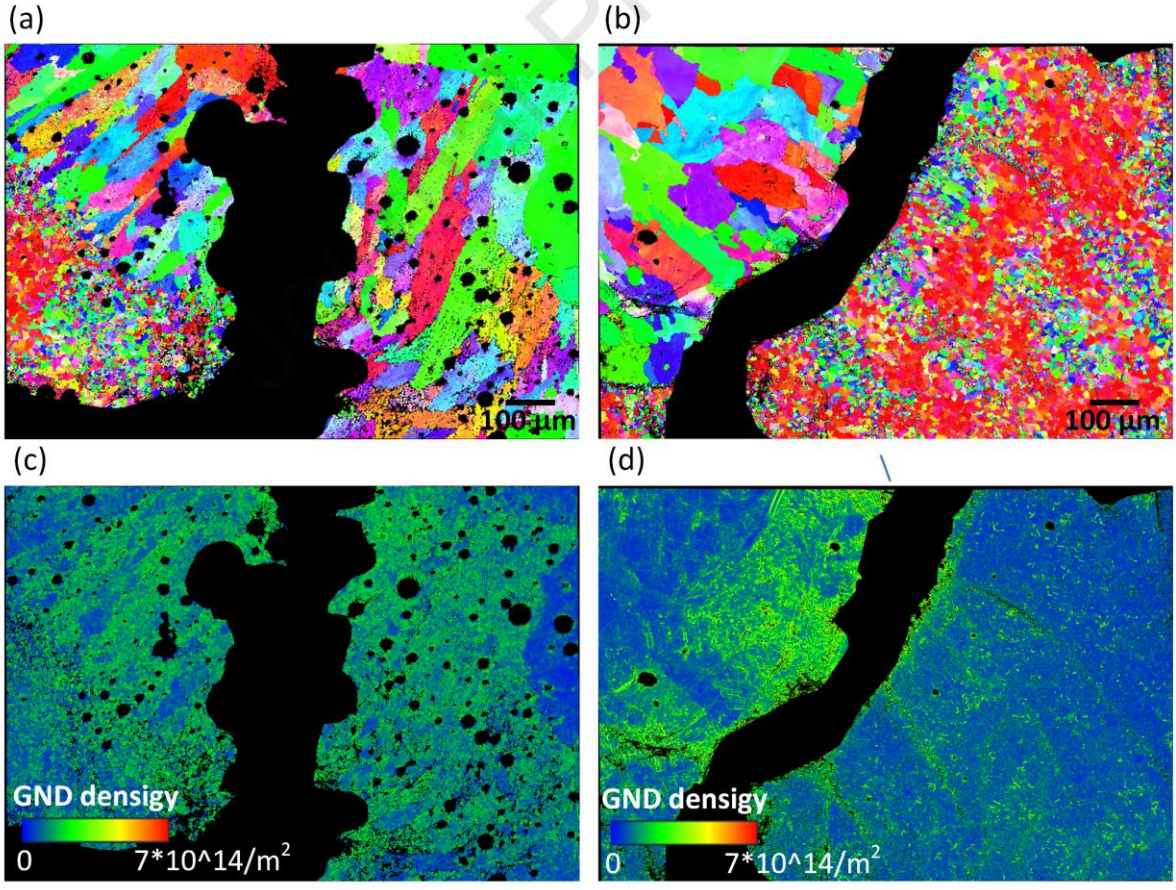

Fig. 12. EBSD map at the failure position after lap-shear tensile test in welds produced with beam oscillation width of 2 mm (a) AM AlSi10Mg sheet on the top and AA1050 sheet at the bottom, and (b) AA1050 sheet on the top and AM AlSi10Mg sheet at the

bottom. (c) and (d) shows the Geometrically Necessary Dislocations (GND) density map in (a) and (b) respectively.

3.5 Effect of placement configuration on the porosity formation

Weld porosity within the fusion zone can be mainly classified into keyhole porosity and hydrogen porosity for the welding of AM materials [5], while the later, in the form of small diameter and dense distribution, is the dominant type as illustrated in Fig. 5. The effect of placement configuration on the formation of hydrogen porosity is discussed in Fig. 13 for the case of partial penetration, with the specific focus on the difference in thermal and chemical composition distribution. Note that consistent welding parameters are considered in two placement configurations and the difference in the weld penetration is related to the various laser energy absorption rates of the two materials, as reflected in Fig. 3 and Fig. 4. It is believed that the origin of the pores during the laser welding is related to the separation of hydrogen dissolved in the AM AlSi10Mg sheet and the existing pores in the as-printed material [13]. Hence, more bubbles are expected in the molten pool of the weld with AM AlSi10Mg positioned on top due to a higher proportion of molten material originating from AM AlSi10Mg. Once generated in the molten pool ((a-i) and (b-i)), these small bubbles would rise and grow by merging with adjacent pores [35]. It should be addressed that a greater fluid flow is expected in the weld with AM AlSi10Mg sheet on top because of first, the higher temperature associated with the higher laser energy absorption rate of AM AlSi10Mg, and secondly, the reduced viscosity of the molten material resulting from the higher Si content in the molten pool (as shown in Fig. 9) [36]. This greatly promotes the floating-up of the bubbles in Fig. 13 (a), which enhances the coalesce and growth of the small bubbles. As the solidification proceeds (step (ii)-(iv)), the bubbles remaining in the solidified material form the pores in the fusion zone. It has been reported in [26,28] that an increase in the Si content can extend the solidification range of aluminium alloy by lowering the melting temperature. In addition, considering a higher thermal distribution, a longer solidification time is assumed when placing the AM AlSi10Mg sheet on top (a-iv), leading to a greater possibility of pore growth. Consequently, a higher quantity and larger scale of pores, are expected when the AM AlSi10Mg is on top (Fig. 5(b) and Fig. 13 (a-iv)), as compared to Fig. 5 (e) and Fig. 13 (b-iv).

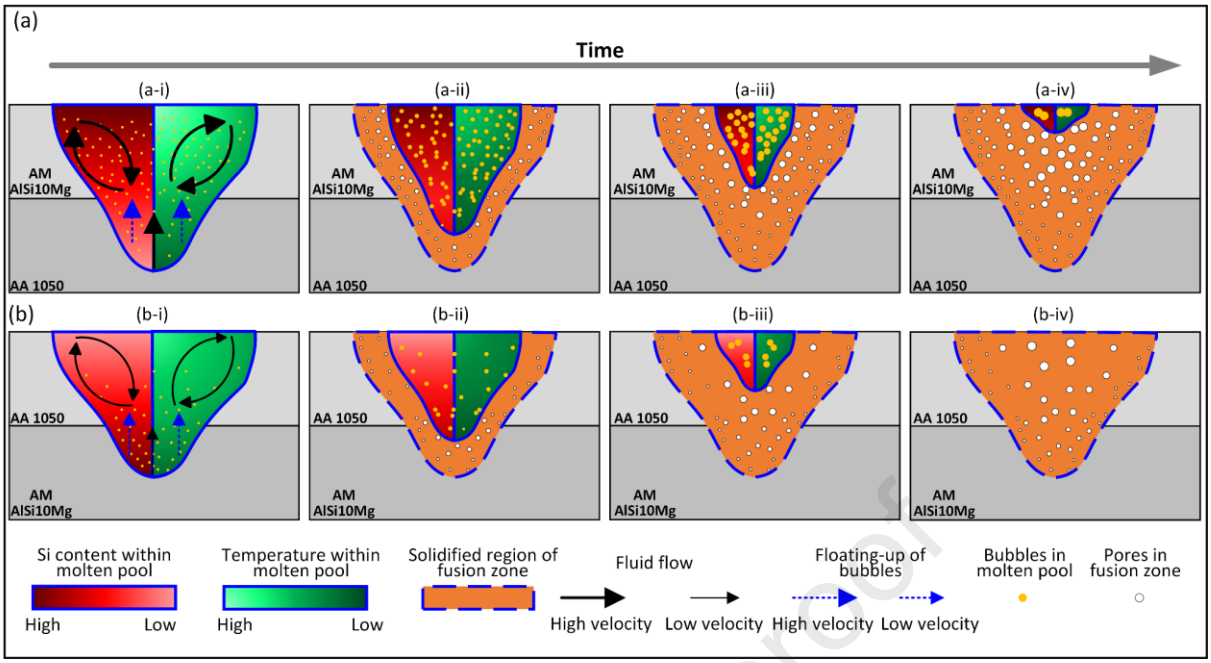

Fig. 13. Schematic diagram demonstrating the formation process of hydrogen porosity in the placement configuration of (a) AM AlSi10Mg sheet on the top and AA1050 sheet at the bottom, and (b) AA1050 sheet on the top and AM AlSi10Mg sheet at the bottom. (i) refers to the time that laser beam is exactly above the molten pool, and (ii)-(iv) refer to the solidification process after laser beams passes. Note that schematic illustrations of the Si content and temperature in the molten pool were plotted in the half volume of the molten pool, respectively for a better visualization. The fluid flow and floating-up of the bubbles in (ii)- (iv) were omitted.

4. Conclusions

In this study, the effect of placement configuration on the weld microstructure, porosity formation and weld mechanical property during laser welding of AM AlSi10Mg alloy and conventionally manufactured 1050 aluminium alloy was investigated. The effect of placement configuration was also study in cases ranging from full penetration to partial penetration, achieved by welding with constant power but varying laser beam oscillation widths. The main findings are summarized below:

- Alternating the placement configuration leads to great changes in the weld geometry and microstructural features. When positioning the AM AlSi10Mg sheet on top, higher weld penetration and higher Si content within the molten pool, especially in the upper sheet, were observed. Additionally, welds with the AM AlSi10Mg sheet on top exhibited more equiaxed grains in the weld centre and refined columnar grains near the fusion boundary of the upper sheet.
- Pores were determined within the entire fusion zone for both placement configurations and a substantially greater number of pores and larger pore diameter were observed in the upper sheet, due to the longer solidification time that facilitates the growth of pores. Significant reductions in the area fraction of weld porosity were observed by positioning the AM AlSi10Mg sheet at the bottom (3.2%~7.2%) compared to placing it on top (16.9%~20.1%), regardless of the weld penetration. This can be attributed to the fact that the hydrogen

bubbles originating from the AM AlSi10Mg sheet experienced a shorter time in the molten pool, restricting the merging and growth of small bubbles.

- All welds failed in the AM AlSi10Mg sheet during the lap-shear tensile test for both placement configurations Failure occurred transgranularly across the columnar grains in the fusion zone when the AM AlSi10Mg sheet was on top, while it occurred intergranularly along the fusion boundary with the AM AlSi10Mg at the bottom. A slightly lower joint strength was observed in welds with the AM AlSi10Mg sheet at the bottom, potentially due to the plastic deformation incompatibility between large columnar grains in the fusion zone and the fine grains in the as-printed material, resulting in significant strain concentration in the columnar grains.

Acknowledgements

This work was financially supported by (1) WMG HVM Catapult; (2) APC UK project: ALIVE - Aluminium Intensive Vehicle Enclosures; (3) Innovate UK IDP15 project LIBERATE: Lightweight Innovative Battery Enclosures using Recycled Aluminium Technologies; and (4) Innovate UK FASA: Flexible, Automated Stator Assembly. The authors also would like to acknowledge the support by the WMG characterisation Facility, partially funded by Higher Education Funding Council for England (HEFCE) and the WMG Centre High Value Manufacturing Catapult. The X-Ray Computed Tomography (XCT) data used in this article was acquired using the Free-at-Point-of-Access scheme at the National Facility for X-Ray Computed Tomography (NXCT) and carried out at the Centre for Imagine, Metrology, and Additive Technologies (CiMAT) at the University of Warwick under the EPRSC Project Number (EP/T02593X/1).

References

[1] Silbernagel C, Ashcroft I, Dickens P, Galea M. Electrical resistivity of additively manufactured AlSi10Mg for use in electric motors. Addit Manuf 2018;21:395–403. https://doi.org/10.1016/j.addma.2018.03.027.

[2] Möller B, Schnabel K, Wagener R, Kaufmann H, Melz T. Fatigue assessment of additively manufactured AlSi10Mg laser beam welded to rolled EN AW-6082-T6 sheet metal. Int J Fatigue 2020;140:105805. https://doi.org/10.1016/j.ijfatigue.2020.105805.

[3] Brock L, Ogunsanya I, Asgari H, Patel S, Vlasea M. Relative Performance of Additively Manufactured and Cast Aluminum Alloys. J Mater Eng Perform 2021;30:760–82. https://doi.org/10.1007/s11665-020-05403-7.

[4] Sun T, Franciosa P, Sokolov M, Ceglarek D. Challenges and opportunities in laser welding of 6xxx high strength aluminium extrusions in automotive battery tray construction. Procedia CIRP 2020;94:565–70. https://doi.org/10.1016/j.procir.2020.09.076.

[5] Minhas N, Sharma V, Bhadauria SS. A review on weldability and corrosion behaviour of L-PBF printed AlSi10Mg alloy. Can Metall Q 2023;62:262–94. https://doi.org/10.1080/00084433.2022.2111968.

[6] Vilaro T, Abed S, Knapp W. Direct manufacturing of technical parts using selective laser melting: example of automotive application. Proc. 12th Eur. Forum Rapid Prototyp., vol. 2, 2008.

[7] Schwarz A, Schleser M, Gerhards B, Popoola P, Gebhardt A. Welding of Additive Manufactured ALSI10MG: Using Laser Welding in a Vacuum for High Quality Weld Seams—A New Approach to Welding LPBF Manufactured ALSI10MG. South African J Ind Eng 2021;32:99–112.

[8] Du Z, Tan MJ, Chen H, Bi G, Chua CK. Joining of 3D-printed AlSi10Mg by friction stir welding. Weld World 2018;62:675–82. https://doi.org/10.1007/s40194-018-0585-7.

[9] Du Z, Chen HC, Tan MJ, Bi G, Chua CK. Investigation of porosity reduction, microstructure and mechanical properties for joining of selective laser melting fabricated aluminium composite via friction stir welding. J Manuf Process 2018;36:33–43. https://doi.org/10.1016/j.jmapro.2018.09.024.

[10] Moeini G, Sajadifar S V., Wegener T, Rössler C, Gerber A, Böhm S, et al. On the influence of build orientation on properties of friction stir welded Al-Si10Mg parts produced by selective laser melting. J Mater Res Technol 2021;12:1446–60. https://doi.org/10.1016/j.jmrt.2021.03.101.

[11] Nahmany M, Hadad Y, Aghion E, Stern A, Frage N. Microstructural assessment and mechanical properties of electron beam welding of AlSi10Mg specimens fabricated by selective laser melting. J Mater Process Technol 2019;270:228–40. https://doi.org/10.1016/j.jmatprotec.2019.02.025.

[12] Nahmany M, Rosenthal I, Benishti I, Frage N, Stern A. Electron beam welding of AlSi10Mg workpieces produced by selected laser melting additive manufacturing technology. Addit Manuf 2015;8:63–70. https://doi.org/10.1016/j.addma.2015.08.002.

[13] Zhang C, Bao Y, Zhu H, Nie X, Zhang W, Zhang S, et al. A comparison between laser and TIG welding of selective laser melted AlSi10Mg. Opt Laser Technol 2019;120:105696. https://doi.org/10.1016/j.optlastec.2019.105696.

[14] Sun T, Franciosa P, Ceglarek D. Effect of focal position offset on joint integrity of AA1050 battery busbar assembly during remote laser welding. J Mater Res Technol 2021;14:2715–26. https://doi.org/10.1016/j.jmrt.2021.08.002.

[15] Sun T, Mohan A, Liu C, Franciosa P, Ceglarek D. The impact of Adjustable-Ring-Mode (ARM) laser beam on the microstructure and mechanical performance in remote laser welding of high strength aluminium alloys. J Mater Res Technol 2022;21:2247–61. https://doi.org/10.1016/j.jmrt.2022.10.055.

[16] Pamarthi VV, Sun T, Das A, Franciosa P. Tailoring the weld microstructure to prevent solidification cracking in remote laser welding of AA6005 aluminium alloys using adjustable ringmode beam. J Mater Res Technol 2023;25:7154–68. https://doi.org/10.1016/j.jmrt.2023.07.154.

[17] Biffi CA, Fiocchi J, Tuissi A. Laser Weldability of AlSi10Mg Alloy Produced by Selective Laser Melting: Microstructure and Mechanical Behavior. J Mater Eng Perform 2019;28:6714–9. https://doi.org/10.1007/s11665-019-04402-7.

[18] Sun T, Ferguson N, Liu C, Gibbons G, Franciosa P. Application of adjustable ring mode laser in remote laser welding of additive manufactured AlSi10Mg alloy Application of adjustable ring mode laser in remote laser welding of additive manufactured AlSi10Mg alloy 2022;042007. https://doi.org/10.2351/7.0000794.

[19] Dimatteo V, Liverani E, Ascari A, Fortunato A. Weldability and mechanical properties of dissimilar laser welded aluminum alloys thin sheets produced by conventional rolling and Additive Manufacturing. J Mater Process Technol 2022;302:117512. https://doi.org/10.1016/j.jmatprotec.2022.117512.

[20] Chen L, Wang C, Xiong L, Zhang X, Mi G. Microstructural, porosity and mechanical properties of lap joint laser welding for 5182 and 6061 dissimilar aluminum alloys under different place configurations. Mater Des 2020;191:108625. https://doi.org/10.1016/j.matdes.2020.108625.

[21] Chianese G, Franciosa P, Sun T, Ceglarek D, Patalano S. Using photodiodes and supervised machine learning for automatic classification of weld defects in laser welding of thin foils copper-to-steel battery tabs. J Laser Appl 2022;34.

https://doi.org/10.2351/7.0000800.

[22] ISO EN. 6892-1. Metallic materials-Tensile testing-Part 1: Method of test at room temperature. Int Organ Stand 2009.

[23] Li Y, Wang F, Liu H, Yang L, Zhang P, Wang Y, et al. Effect of surface roughness on the performances of laser-welded Invar 36 alloy joints. Opt Laser Technol 2023;162:109307. https://doi.org/10.1016/j.optlastec.2023.109307.

[24] Bolzoni L, Hari Babu N. Engineering the heterogeneous nuclei in Al-Si alloys for solidification control. Appl Mater Today 2016;5:255–9. https://doi.org/10.1016/j.apmt.2016.11.001.

[25] Kimura R, Hatayama H, Shinozaki K, Murashima I, Asada J, Yoshida M. Effect of grain refiner and grain size on the susceptibility of Al-Mg die casting alloy to cracking during solidification. J Mater Process Technol 2009;209:210–9. https://doi.org/10.1016/j.jmatprotec.2008.01.053.

[26] Montero Sistiaga ML, Mertens R, Vrancken B, Wang X, Van Hooreweder B, Kruth JP, et al. Changing the alloy composition of Al7075 for better processability by selective laser melting. J Mater Process Technol 2016;238:437–45. https://doi.org/10.1016/j.jmatprotec.2016.08.003.

[27] Aboulkhair NT, Tuck C, Ashcroft I, Maskery I, Everitt NM. On the Precipitation Hardening of Selective Laser Melted AlSi10Mg. Metall Mater Trans A Phys Metall Mater Sci 2015;46:3337–41. https://doi.org/10.1007/s11661-015-2980-7.

[28] Abdel-Jaber GT, Omran AM, Khalil KA, Fujii M, Seki M, Yoshida A. An investigation into solidification and mechanical properties behavior of Al-Si casting alloys. Int J Mech Mech Eng 2010;10:34–41.

[29] Dwivedi DK, Sharma R, Kumar A. Influence of silicon content and heat treatment parameters on mechanical properties of cast Al-Si-Mg alloys. Int J Cast Met Res 2006;19:275–82. https://doi.org/10.1179/136404606X153867.

[30] Ning J, Hong KM, Inamke G V., Shin YC, Zhang LJ. Analysis of microstructure and mechanical strength of lap joints of TZM alloy welded by a fiber laser. J Manuf Process 2019;39:146–59. https://doi.org/10.1016/j.jmapro.2019.02.015.

[31] Li X, Lu L, Li J, Zhang X, Gao H. Mechanical properties and deformation mechanisms of gradient nanostructured metals and alloys. Nat Rev Mater 2020;5:706–23. https://doi.org/10.1038/s41578-020-0212-2.

[32] Hu YN, Wu SC, Chen L. Review on failure behaviors of fusion welded high-strength Al alloys due to fine equiaxed zone. Eng Fract Mech 2019;208:45–71. https://doi.org/10.1016/j.engfracmech.2019.01.013.

[33] Hu K, Muneer W, Zhang J, Zhan X. Effect of beam oscillating frequency on the microstructure and mechanical properties of dissimilar laser welding of AA2060 and AA6061 alloy. Mater Sci Eng A 2022;832. https://doi.org/10.1016/j.msea.2021.142431.

[34] Chen L, Hu YN, He EG, Wu SC, Fu YN. Microstructural and failure mechanism of laser welded 2A97 Al–Li alloys via synchrotron 3D tomography. Int J Light Mater Manuf 2018;1:169–78. https://doi.org/10.1016/j.ijlmm.2018.08.001.

[35] Chen N, Wan Z, Wang HP, Li J, Yang B, Solomon J, et al. Effect of ambient pressure on laser welding of AlSi10Mg fabricated by selected laser melting.

Mater Des 2022;215:110427. https://doi.org/10.1016/j.matdes.2022.110427.

[36] Zhao H, White DR, Debroy T. Current issues and problems in laser welding of automotive aluminum alloys. Int Mater Rev 1999;44:238–66. https://doi.org/10.1179/095066099101528298.

Declaration of interests

☒ The authors declare that they have no known competing financial interests or personal relationships that could have appeared to influence the work reported in this paper.

☐ The authors declare the following financial interests/personal relationships which may be considered as potential competing interests: